Journal of Volcanology and Geothermal Research 325 (2016) 61–69

Contents lists available at ScienceDirect

Journal of Volcanology and Geothermal Research

journal homepage: www.elsevier.com/locate/jvolgeores

Drone with thermal infrared camera provides high resolution georeferenced imagery of the Waikite geothermal area, New Zealand

M.C. Harvey [a,*], J.V. Rowland [a], K.M. Luketina [b]

[a] School of Environment, University of Auckland, Auckland, New Zealand
[b] Waikato Regional Council, Private Bag 3038, Waikato Mail Centre, Hamilton 3240, New Zealand

ARTICLE INFO

Article history:
Received 5 April 2016
Received in revised form 17 June 2016
Accepted 18 June 2016
Available online 21 June 2016

Keywords:
Thermal
Infrared
Geothermal
Exploration
Camera
Drone
Uav
Rpas
New Zealand
Monitoring
Photogrammetry
Structure
Motion
Heat
Flow
Flux

ABSTRACT

Drones are now routinely used for collecting aerial imagery and creating digital elevation models (DEM). Lightweight thermal sensors provide another payload option for generation of very high-resolution aerial thermal orthophotos. This technology allows for the rapid and safe survey of thermal areas, often present in inaccessible or dangerous terrain. Here we present a 2.2 km^2 georeferenced, temperature-calibrated thermal orthophoto of the Waikite geothermal area, New Zealand. The image represents a mosaic of nearly 6000 thermal images captured by drone over a period of about 2 weeks. This is thought by the authors to be the first such image published of a significant geothermal area produced by a drone equipped with a thermal camera. Temperature calibration of the image allowed calculation of heat loss (43 ± 12 MW) from thermal lakes and streams in the survey area (loss from evaporation, conduction and radiation). An RGB (visible spectrum) orthomosaic photo and digital elevation model was also produced for this area, with ground resolution and horizontal position error comparable to commercially produced LiDAR and aerial imagery obtained from crewed aircraft. Our results show that thermal imagery collected by drones has the potential to become a key tool in geothermal science, including geological, geochemical and geophysical surveys, environmental baseline and monitoring studies, geotechnical studies and civil works.

1. Introduction

Photogrammetry is a technology that allows the reconstruction of three dimensional information (i.e. Digital Elevation Models) from a mosaic of overlapping, two dimensional photographs (Westoby et al., 2012). Although photogrammetry is not a new technology, recent advances in Unmanned Aerial Vehicle (UAV or drones) equipped with global positioning systems (GPS) and digital cameras have reduced the cost of collecting imagery. Modern desktop and cloud computing power allows for routine post processing of large numbers of individual image photos. The individual photos are combined into aerial orthophotos and Digital Elevation Models (DEM) of comparable quality (<0.1 m) to airborne LiDAR (Harwin and Lucieer, 2012; Fonstad et al., 2013).

In volcanology, UAV were used previously as a sensor platform for data collection in volcanic plumes (McGonigle et al., 2008). Lightweight thermal sensors provide another payload option for generation of very high resolution aerial thermal orthophotos. This technology promises to allow the rapid and safe survey of thermal areas, often present in inaccessible or dangerous terrain.

In this study we provide results from a thermal infrared radiation (TIR) and Red Green Blue (RGB) survey of the Waikite Valley thermal area, New Zealand. The survey was undertaken using a UAV equipped with a point-and-shoot digital camera for standard visible images (RGB), and a thermal infrared camera. The Waikite survey area is administered by the New Zealand Department of Conservation (DOC) and comprises a topographically steep and partly inaccessible valley of regenerating native wetland vegetation within the Waikite geothermal area. Thermal features are associated with the active Paeroa Fault (Berryman et al., 2008) and include high flow-rate boiling springs in the south, warm lakes in the north, hot seeps and steaming ground (Glover et al., 1992). Thermal wetlands in the Waikite Valley are of ecological interest and have been the focus of recent environmental restoration efforts (Reeves et al., 2011). Advective heat loss from the Waikite Valley was previously estimated from the temperature and flow of the

* Corresponding author.
E-mail address: mark@harveygeoscience.co.nz (M.C. Harvey).

http://dx.doi.org/10.1016/j.jvolgeores.2016.06.014
0377-0273/

Fig. 1. DJI Phantom 2 Vision Plus quadcopter modified with ICI thermal camera and UAV module.

Otamakokore thermal stream, which comprises nearly all surface outflow from the survey area (43 MW, Glover et al., 1992) (46 MW; Healy, 1952).

The Waikite geothermal area was previously imaged with a thermal camera carried by crewed helicopter (Bromley, 1992). The purpose of this study was to assess the usefulness of drone technology for finding warm springs or other thermal features in difficult terrain such as wetlands and dense scrub, and to provide an estimate of surface heat loss from thermal water in the survey area.

2. Methods

2.1. Field methods

Imagery was collected using a modified DJI Phantom 2 Vision + quadcopter (Fig. 1). The quadcopter was modified by the replacement of the stock camera with an ICI 640 × 480 uncooled thermal sensor (spectral response 7–14 μm) with automated image capture (ICI UAV module®). A Canon S100 point-and-shoot camera was fitted for normal visible (RGB) and DEM outputs (Harvey et al., 2014).

An appropriate flight plan was determined using UgCS® software running on a Hewlett Packard laptop running Windows 7®. The flight plan was then uploaded to the quadcopter's flight controller via a Samsung S4 smartphone running Android and the UgCS® mobile companion App. Accordingly, both in-flight navigation and image capture were autonomous.

Calibration of the thermal imagery was by direct measurement of water on the ground using a type-K thermocouple temperature probe; measurement of hot pools and nearby cold pools (farm troughs) was made immediately after each mornings flying, which allowed raw pixel response values from the thermal camera to be calibrated for a range of ambient conditions. No water surfaces were affected by direct sunlight during periods of image capture or calibration measurement. This minimized temperature changes in the pools between the time of TIR image capture and ground measurement.

Ground control points (GCP) were established prior to flight so the resulting imagery could be accurately georeferenced. GCP included 19 reflective plastic sheets (1.5 × 2 m) placed at the perimeter of the planned survey area (Fig. 6). The location of the sheets (centre of the sheet) was recorded using Leica RTK GPS equipment with accuracy of 2–3 cm.

2.2. Image processing and analysis

Two-dimensional Thermal and RGB images were converted to 3-dimensional point clouds using Agisoft Photoscan® commercial photogrammetry software, running on a Hewlett Packard laptop computer equipped with an i7 processor and 32GB RAM. Processing provided georeferenced, thermal and RGB raster orthophotos, and a DEM (Table 1).

Raster imagery was analysed and post-processed using QGIS open-source desktop geographic information system (GIS). Post processing steps included conversion of the raw pixel values to calibrated temperature values (°C), and then to heat flux values (W m^{-2}), as described below.

2.3. Estimation of heat loss

Areas of surface thermal water (lakes, streams) were selected from temperature calibrated raster images. For this purpose, the QGIS Raster Calculator tool was used to select pixels above the ambient temperature (8–16 °C). Mean heat loss (W m^{-2}) from these areas was estimated using deterministic heat flow equations (2.3.1–2.3.3) (Dawson, 1964; Dawson and Dickinson, 1970; Sorey and Colvard, 1994; Fridriksson et al., 2006) within a stochastic Monte Carlo simulation (Robert and Casella, 2013) developed in Microsoft Excel (2.3.4); randomly generated climatic data provided ambient conditions required by the equations (ambient air temperature, wind speed, humidity, air pressure).

Heat loss from the water's surface has several components including loss from (1) evaporation, (2) conduction through air (3) radiation and (4) ebullition (boiling). For vigorously boiling pools, a significant proportion may be due to steam passing through the water, but ebullition cannot be quantified from aerial thermal imagery and this fraction of heat loss was not considered. However, nearly all of the surface area of thermal water in the survey area was <80 °C (>99.9%), so this fraction is likely to be relatively minor.

2.3.1. Evaporative heat loss from streams and lakes

The heat loss from pools by evaporation is obtained by the following equations from Fridriksson et al. (2006):

$$H_e = A\,(h_V - h_L)\,(0.0065 + 0.0029\,w) \times (P_{H2O\ TP} - P_{H2O\ ATM})/P_{TOT}$$

where:

A (m^2) = surface area of pool

h_V (J/kg) = steam enthalpy at pool temperature

h_L (J/kg) = liquid water enthalpy at pool temperature

w (m/s) = wind speed (m/s)

$P_{H2O\ TP}$ (bar) = H_2O vapour pressure of water at pool temperature

$P_{H2O\ ATM}$ (bar) = H_2O vapour pressure at local atmospheric temperature and humidity

P_{TOT} (bar) = atmospheric pressure.

Table 1
Image processing output.

Description	Ground resolution (m)	RMS error (m)	Area (km^2)	Computer processing time (hours)
Temperature calibrated thermal orthophoto	0.19	~1 (x), ~1 (y)	2.2	48
Georeferenced RGB orthophoto	0.04	0.11 (x), 0.07(y)	3.0	70
Georeferenced DEM	0.17	0.11 (x), 0.07(y), 0.24 (z)	3.0	–

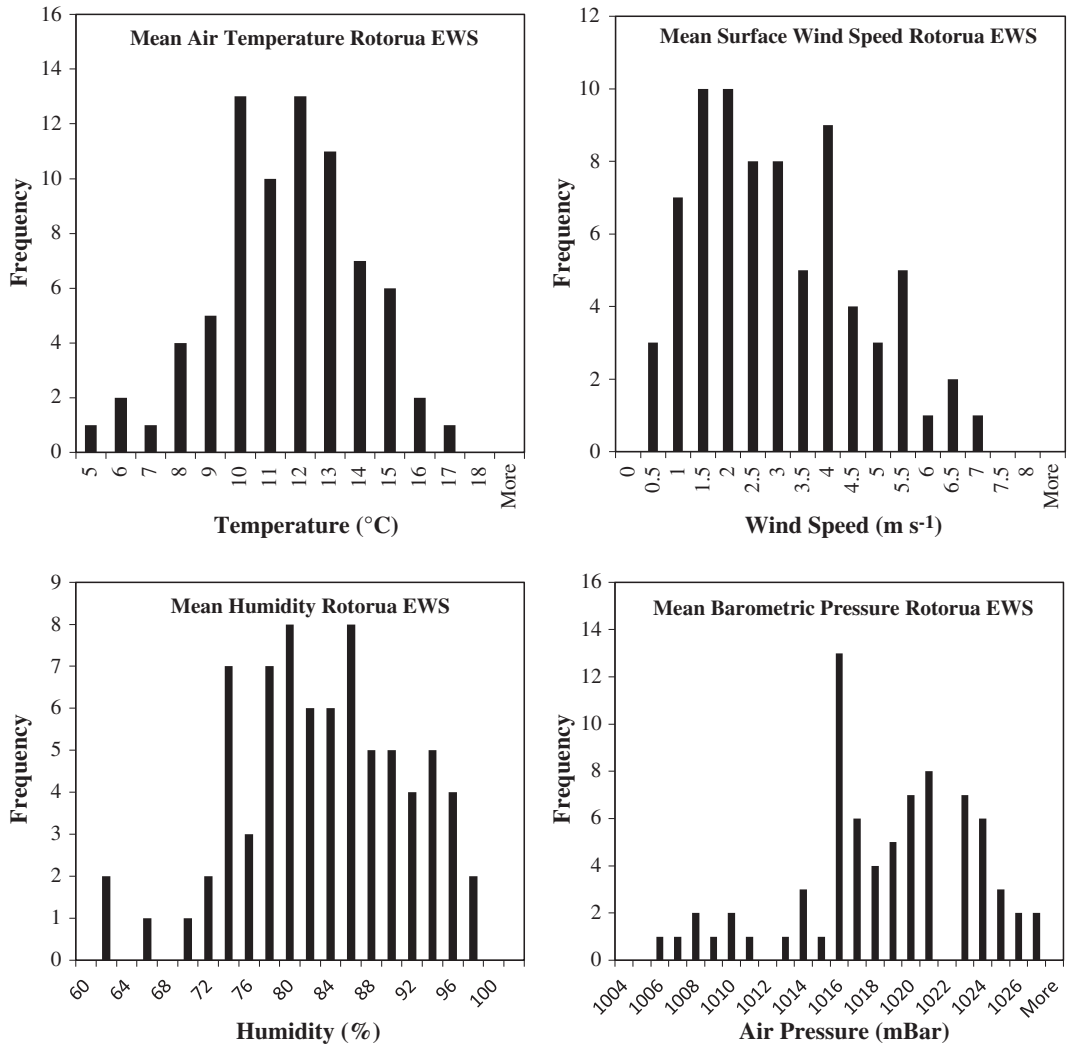

Fig. 2. Hourly meteorological observations recorded Rotorua EWS weather station during the survey period 14th October and 2nd November 2015, between 6 and 10 am (time of flights).

2.3.2. Conductive heat loss

Conductive heat loss is obtained as a ratio with respect to evaporative heat loss (Fridriksson et al., 2006):

$$\text{RB (Bowen Ratio)} = H_c/H_e = 6.1 \times 10^{-4}\, P_{TOT}\, (t_P - t_{ATM})/(P_{H2O\ TP} - P_{H2O\ ATM}).$$

where:

T_P (deg K) = pool temperature

T_{ATM} (deg K) = local atmospheric temperature

$P_{H2O\ TP}$ (bar) = H_2O vapour pressure of water at pool temperature

$P_{H2O\ ATM}$ (bar) = H_2O vapour pressure at local atmospheric temperature and humidity

P_{TOT} (bar) = atmospheric pressure.

2.3.3. Heat loss by radiation

The radiation heat loss is obtained using the Stefan-Boltzmann law (Dawson, 1964).

$$H_r = A\varepsilon\sigma \cdot (T^4_P - T^4_{ATM})$$

where:

A = pool area (m^2)

ε = Emissivity constant (0.955)

σ = Stefan-Boltzmann constant (5.68×10^{-8} J/s m^2)

T_P = pool temperature (deg K)

T_{ATM} = air temperature (deg K)

2.3.4. Monte Carlo simulation

Random climate data was generated within Excel by modelling histograms of hourly climatic observations recorded at a fixed meteorological station (Rotorua EWS weather station) (Fig. 2). The station is located ~18 km from the survey area, at a similar elevation (290 m ASL station, compared with 350–460 m for the survey area) (NIWA, 2015). Temperature and wind speed averages and extremes from the weather station agree with field observations providing confidence that station data adequately represent the range of local conditions.

The simulation was repeated for a range of possible pixel temperatures (between 16 and 100 °C, at 4 °C increments), providing mean and standard deviation (s.d.) (W $pixel^{-1}$) heat flux at each increment. Data was plotted (pixel temp versus heat flux) and equations fitted. These equations were used within the QGIS Raster Calculator tool to provide a sum of heat flow for the selected pixels.

The work flow described above was implemented as follows:

1. Obtain histograms for local climatic variables from meteorological station (Fig. 2).

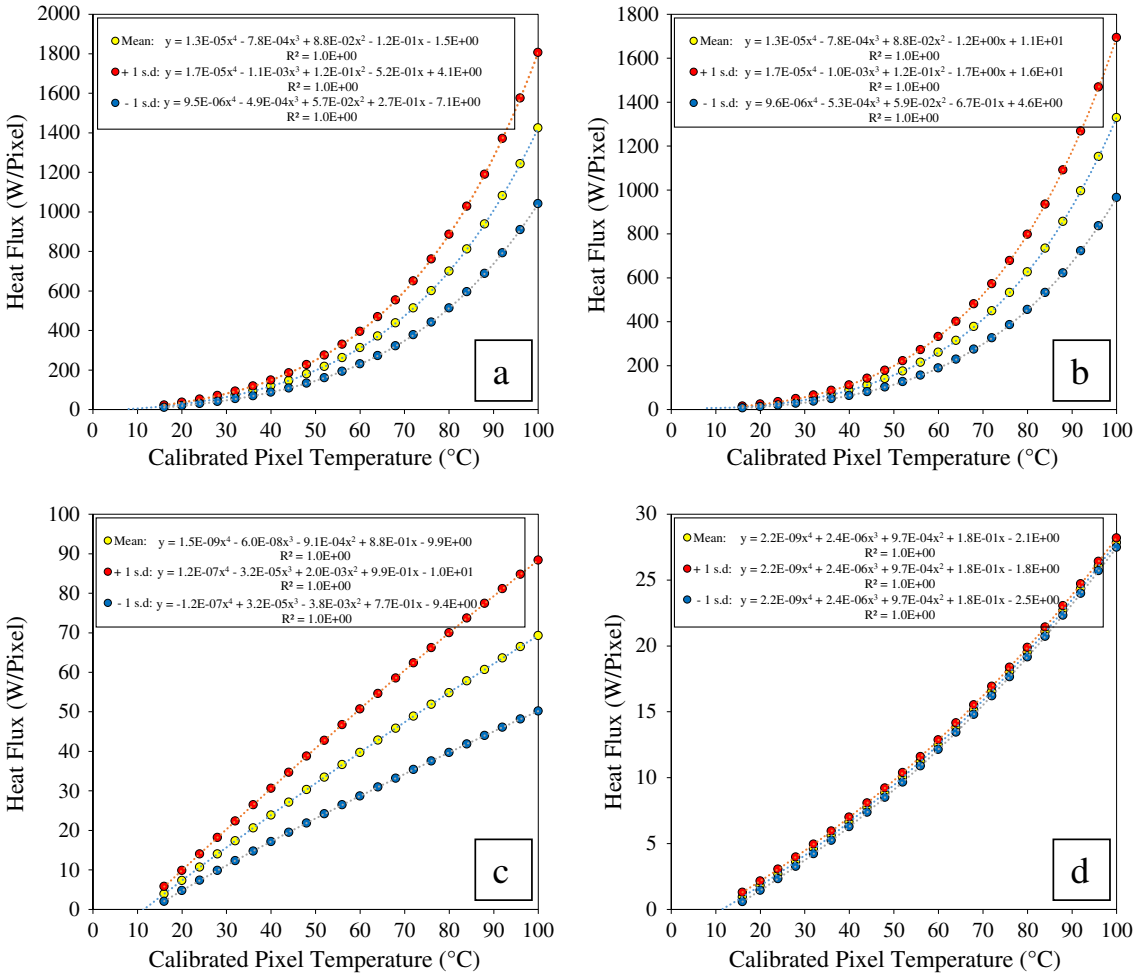

Fig. 3. Monte Carlo simulation results (2×10^4 realisations) for surface heat flux. Pixel temperature versus heat flux (mean ± s.d.) at 4 °C increments (pixel area 0.04m^2). (a) All components (evaporation, conduction and radiation combined), (b) evaporation, (c) conduction, and (d) radiation.

2. Calculate heat flux (W pixel^{-1}) using equations (2.3.1–2.3.3) for a randomly generated set of ambient conditions, for a range of pixel temperature (16–100 °C, 4 °C increments).
3. Simulation: repeat step 2 multiple times (number of realisations).
4. Record statistics from simulation results (heat flux: mean and s.d.) for each component (evaporation, conduction, radiation, total), for each temperature increment.
5. Plot pixel temperature versus heat flux (mean ± s.d.) for each increment, and fit equations (Fig. 3).
6. Input equations to QGIS Raster Calculator tool to obtain total heat flow for selected pixels, for each component (mean ± s.d.) (Table 2).
7. Repeat steps 2–6 multiple times to determine if simulation results (mean) are stable. If not, then increase number of realisations (step 3) and repeat steps 3–7 (Fig. 4).

3. Results

For thermal imagery, 17 flights were made between 14th October and 2nd November 2015. Flight conditions were clear and cool (8–16 °C) in the early morning (between 6 and 10 am), with a maximum wind speed of ~6 m/s. The total flight time was about 200 min, providing 5882 thermal images. Computer post-processing of imagery took about 48 h, providing a thermal orthophoto with a total coverage of ~2.2 km^2 and ground resolution of 19 cm (Fig. 5) (Table 1). Manual cross checking alignment of the thermal orthophoto with the visible orthophoto indicates positional Root Mean Squared Error (RMSE) of 1.0 m for the thermal image (average offset from the visible orthophoto based on 25 evenly distributed check points). Thermal features are clearly identifiable in the thermal orthorectified image.

Table 2
Waikite heat flow (MW).

Area	Evap.		Cond.		Rad.		Total	
	Mean[a]	s.d.[b]	Mean	s.d.	Mean	s.d.	Mean	s.d.
South Waikite	28.7	8.0	8.3	2.4	2.3	0.2	39.3	10.5
North Waikite	2.6	0.9	0.9	0.4	0.2	0.1	3.7	1.4
Total							43.0	11.9

[a] Average heat flow from on Monte Carlo analysis (2×10^5 realisations).
[b] Standard deviation of heat flow based on Monte Carlo analysis (2×10^5 realisations).

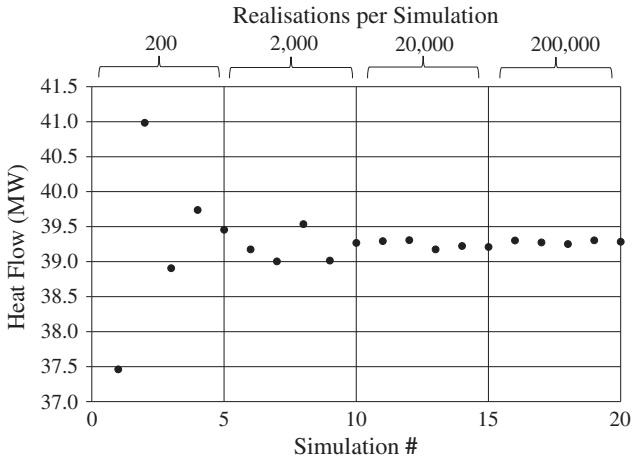

Fig. 4. Mean heat flow for Waikite South estimated from Monte Carlo simulations and QGIS Raster Calculator tool. Note: Simulation heat flow stabilises at 39.3 MW as the number of realisations per simulation increases. Heat flow is for evaporation, conduction and radiation components.

Thermal imagery was calibrated by ground truthing; hot and cold pools of water were measured with a temperature probe just after flying. This has allowed the generation of calibrated and georeferenced thermal imagery that can be investigated in detail and analysed with standard GIS software (ArcGIS, QGIS, etc.). Calibration showed a linear relationship between pixel value and measured temperatures (Fig. 10). Increased scatter was observed at higher temperatures (>80 °C) that may be due to screening by steam. However, the correlation in the cross plot is good ($r^2 = 0.98$), with a standard error of the regression of ±2.3 °C under 80 °C. The regression equation allowed temperature to be estimated for each pixel (Fig. 5).

Lake Puakohurea is expanded in Figs. 8–9 to illustrate the quality of the thermal imagery, and thermal calibration of pixels (see Fig. 10). Fig. 8(a) indicates Lake Puakohurea is warmest (43 °C) where hot springs enter the eastern side, then cools towards the western outflow. Springs at the eastern side were measured previously (47.5 °C; Glover et al., 1992). Fig. 8(b) illustrates the selection of pixels above ambient temperature using the QGIS Raster Calculator tool (2.3), and application of Monte Carlo derived heat flow equations (2.3.1–2.3.4) to these pixels.

Calibrated thermal imagery and Monte Carlo analysis provided surface heat loss (39.3 ± 10.5 MW) for thermal lakes and streams in the southern half of the survey area (including and south of Lake Puakohurea). Lakes and streams in the northern half of the survey area provided a minor component (3.7 ± 1.4 MW) of the total surface heat loss (43.0 ± 11.9 MW) (Table 2).

Of the heat flow components (Table 2), evaporation is dominant, conduction intermediate, and radiation minor, which is consistent with previous reports of heat loss from geothermally heated waters (Brown et al., 1989; Bloomer, 2012).

For the visible imagery and the DEM, 8 flights were made between the 7th and 10th October 2015. Flight conditions were clear and sunny, with maximum wind speed of ~8 m/s. The total flight time was about 120 min, providing 2035 images. Computer post-processing of imagery took about 72 h, providing 33 orthophoto tiles and DEM with a total coverage of ~3 km^2, and orthophoto ground resolution of 4 cm (Figs. 6, 7, 9) (Table 1). Close inspection of the orthophoto allows

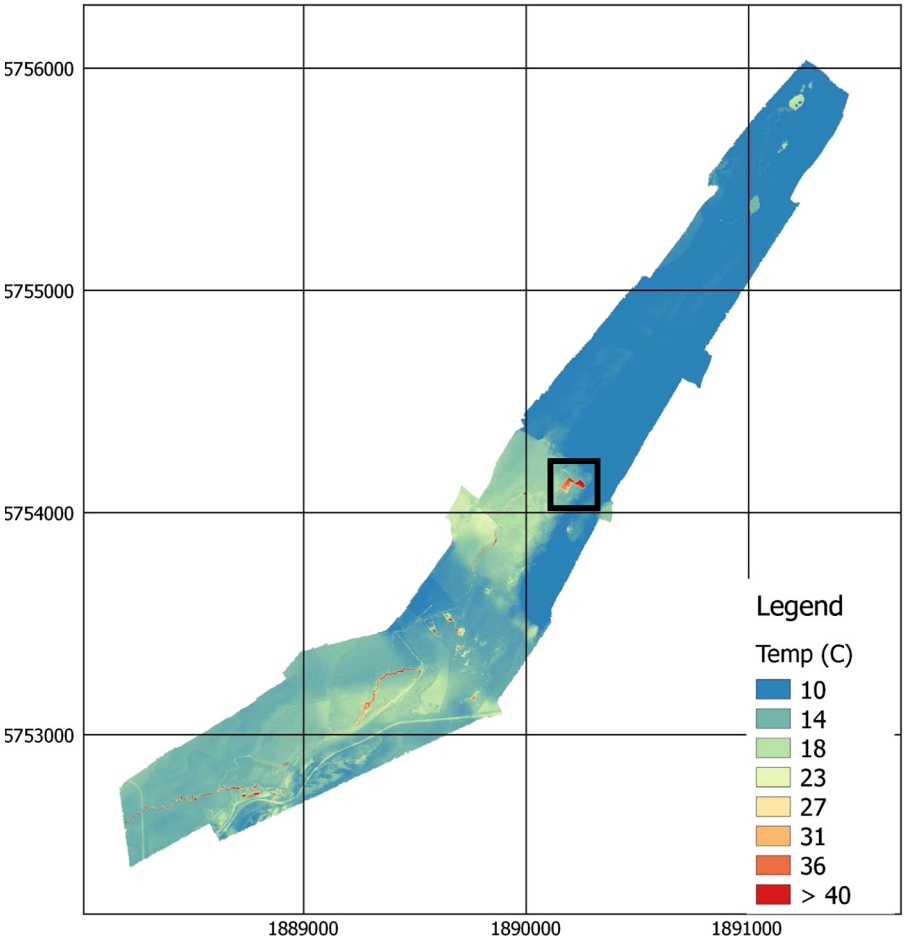

Fig. 5. Waikite calibrated thermal infrared orthophoto. Black box is expanded in Figs. 8–9. Map Datum NZGD2000.

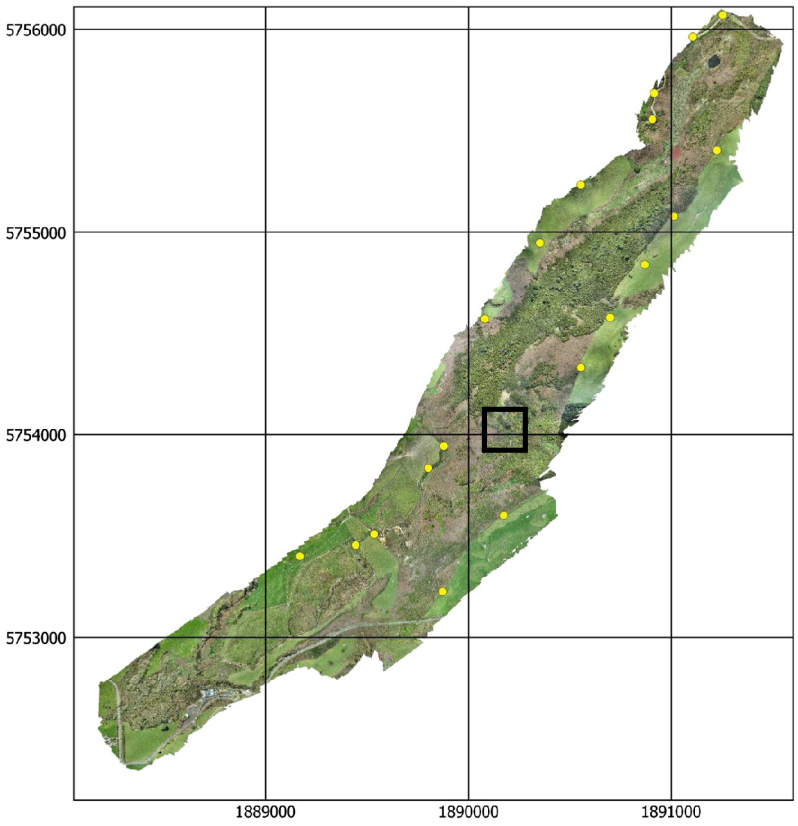

Fig. 6. Waikite RGB orthophoto. Yellow dots show location of ground control points. Area within black box is expanded in Figs. 8–9. Map Datum NZGD2000.

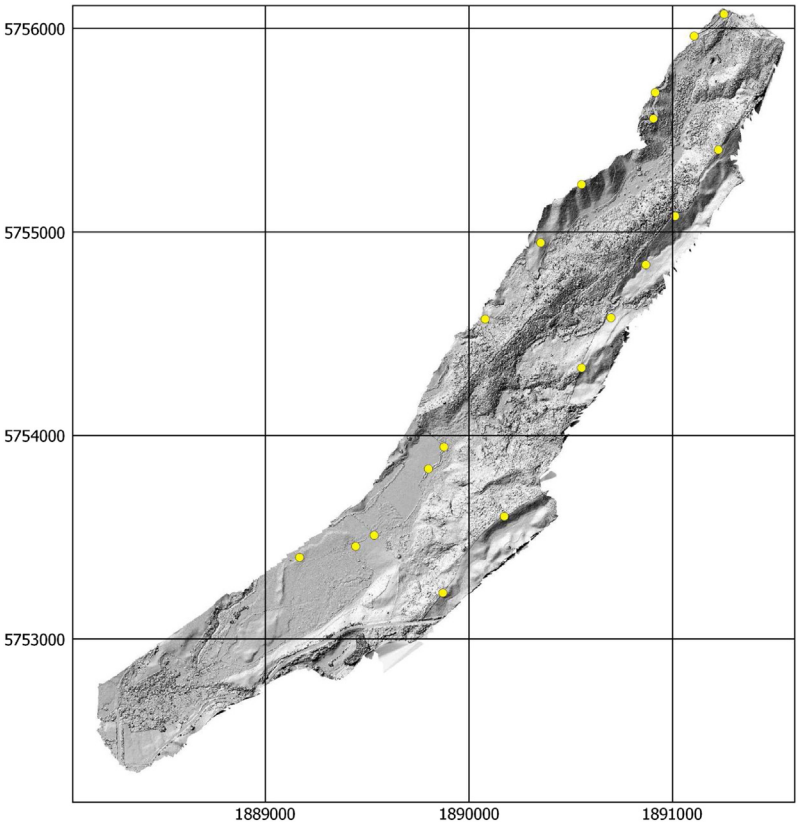

Fig. 7. Waikite digital elevation model (DEM). Yellow dots show location of ground control points. Map Datum NZGD2000.

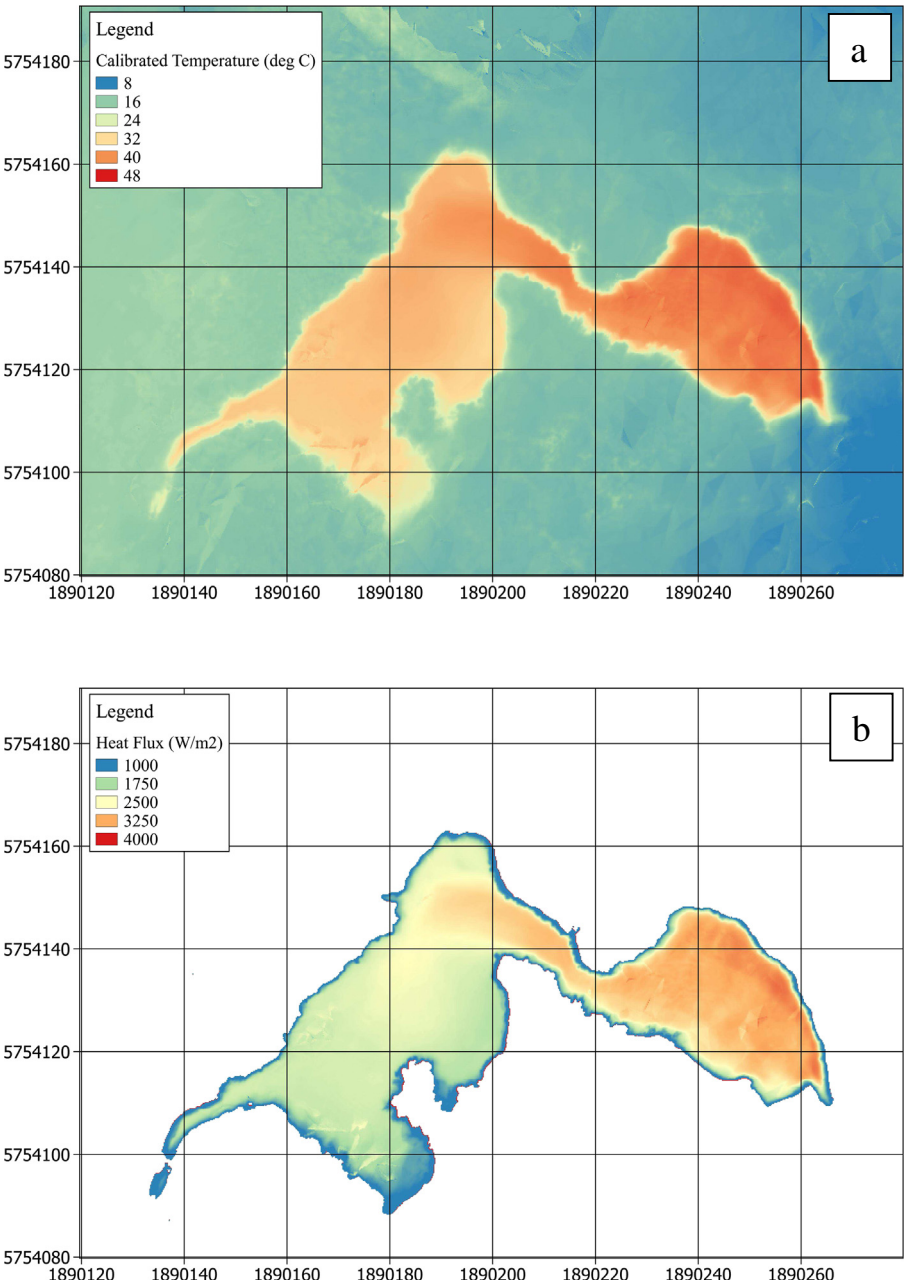

Fig. 8. Expanded area showing (a) temperature calibrated, and (b) heat flux (selected pixels) imagery of Lake Puakohurea in inaccessible terrain (19 cm pixel size) (see black box Fig. 5). Map Datum NZGD2000. Note: Lake is 43 °C where springs inflow (eastern side of the lake), then cools as it flows to the western outflow.

different types of vegetation to be identified (e.g. fern, grass, blackberry, flax). Ground control check points provided positional RMSE (x axis: 11 cm, y axis: 7 cm and z axis: 24 cm).

4. Discussion and conclusions

Recent advances in drone technology, combined with light weight thermal sensors provide a new method for mapping volcanic and geothermal areas at high resolution. However, drone-based studies to date have reported only single thermal images (Amici et al., 2013), or mosaics with limited coverage (700m^2), and no temperature calibration (Nishar et al., 2016). Our results greatly expand upon previous reports in terms of area (2.2 km^2), and by providing temperature calibration, which has allowed an estimate of heat flow.

Our results are important because they show drones provide a viable alternative to crewed aircraft, at least at the scale of this survey. Depending on survey size and drone type, drones may offer a more economic survey platform than crewed aircraft. They are particularly suited to the collection of high resolution imagery, where a low altitude and slow airspeed are necessary.

The temperature calibrated imagery presented here represents a mosaic of nearly 6000 thermal images captured by drone over a period of 2 weeks. To our knowledge, this is the first square-km-scale, temperature calibrated and georeferenced image of a geothermal area ever produced by a drone equipped with a thermal camera. Temperature calibration and georeferencing of imagery provides the potential for more accurate and reproducible surface heat flow surveys of volcanic and geothermal areas. This has many possible applications, including volcanic monitoring (Harris, 2013; Vilardo et al., 2015), environmental monitoring (Allis, 1981; Bromley and Hochstein, 2000; Óladóttir and Friðriksson, 2015), geothermal exploration (Muffler and Cataldi, 1978), and hydrothermal reservoir modelling (O'Sullivan et al., 2001,

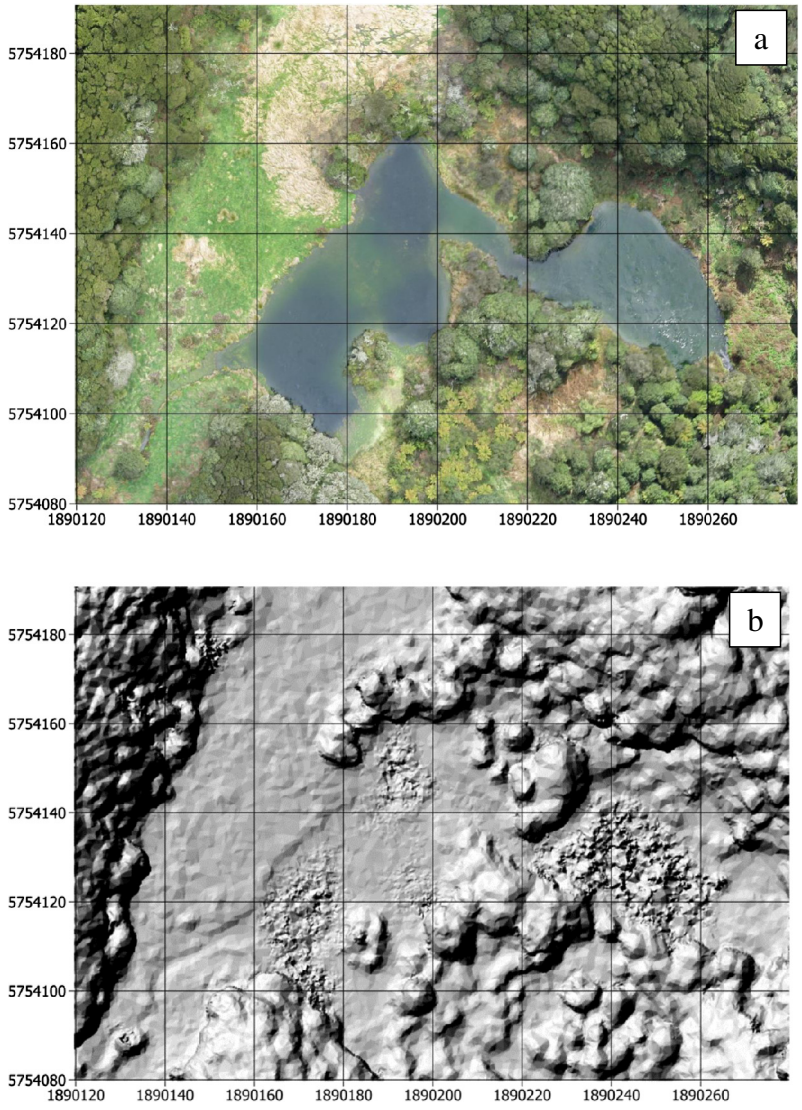

Fig. 9. Expanded area showing high resolution (a) visible imagery, and (b) DEM of Lake Puakohurea in inaccessible terrain (4 cm pixel size) (see black box in Fig. 6). Map Datum NZGD2000. Note: irregular texture of DEM on lake surface is an artifact; generation of 3D point clouds requires a stationary target.

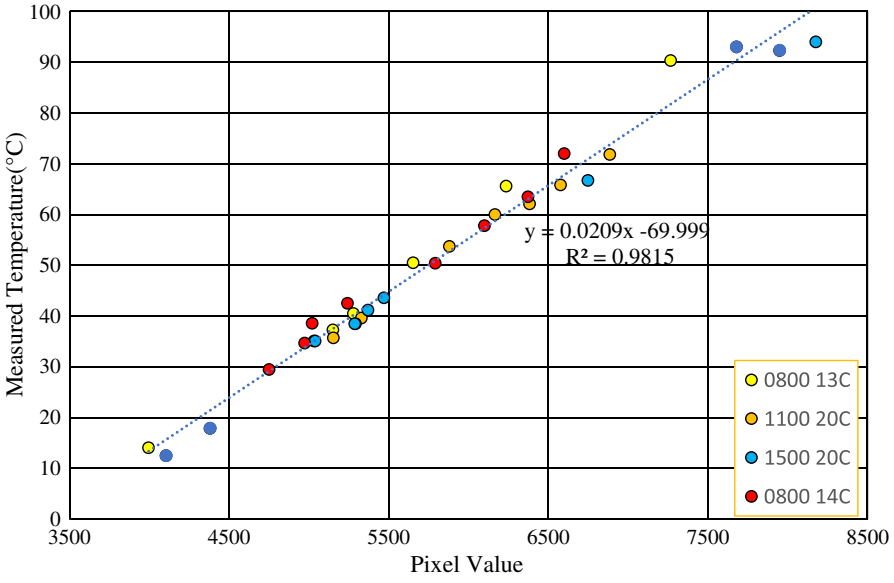

Fig. 10. Thermal camera calibration. Points are colour coded according to the time of day and ambient temperature during calibration flight. Line of best fit and equation are for all points. Standard error = 2.3 °C (for measurements <80 °C). (For interpretation of the references to colour in this figure legend, the reader is referred to the web version of this article.)

2009). Our study demonstrates there are no technical barriers preventing the use of drones to produce accurate thermal and visible maps of large, inaccessible geothermal areas.

For non-thermal imagery, the ground resolution (4 cm) and horizontal position error (~10 cm) are comparable to commercially produced LiDAR and aerial imagery obtained from crewed aircraft.

Calibrated thermal imagery and Monte Carlo analysis provided a mean total surface heat loss of 43 ± 12 MW for thermal lakes and streams in the survey area, during the survey period. The standard deviation (12 MW) results from meteorological variations expected during the survey (ambient air temperature, wind speed, humidity, barometric pressure).

The mean surface heat loss 43 ± 12 MW is a probably a minimum, as a small proportion of thermal water is not visible from above (e.g. obscured by vegetation). This value is for evaporation, conduction and radiation; it does not consider advective heat loss associated with ebullition, or advective heat loss associated with the Otamakokore stream flow (Bibby et al., 1995), which comprises nearly all surface out-flow from the survey area and was quantified previously (43 MW, Glover et al., 1992) (46 MW; Healy, 1952). Assuming a similar heat flow today, the total heat loss for the Waikite survey area averaged ~86 MW during the survey period.

Acknowledgments

We would like to acknowledge the New Zealand Department of Conservation, Penoak Farm, Ngati Tahu-Ngati Whaoa Runanga, Ngati Raukawa, Waikite Valley Thermal Pools, GNS Science, Waikite Landcorp Farm, ICI Cameras and The University of Auckland.

References

Allis, R.G., 1981. Changes in heat flow associated with exploitation of Wairakei geothermal field, New Zealand. N. Z. J. Geol. Geophys. 24 (1), 1–19.
Amici, S., Turci, M., Giulietti, F., Giammanco, S., Buongiorno, M.F., La Spina, A., Spampinato, L., 2013. Volcanic environments monitoring by drones mud volcano case study. Int. Arch. Photogramm. Remote. Sens. Spat. Inf. Sci. 1, W2 UAV.
Berryman, K., Villamor, P., Nairn, I., Van Dissen, R., Begg, J., Lee, J., 2008. Late Pleistocene surface rupture history of the Paeroa fault, Taupo rift, New Zealand. N. Z. J. Geol. Geophys. 51 (2), 135–158.
Bibby, H.M., Glover, R.B., Whiteford, P.C., 1995. The Heat Output of the Waimangu, Waiotapu-Waikite and Reporoa Geothermal Systems (NZ): Do Chloride Fluxes Provide an Accurate Measure? New Zealand Geothermal Workshop 1995 Proceedings.
Bloomer, A., 2012. Heat loss from high temperature ponds. New Zealand Geothermal Workshop 2012 Proceedings.
Bromley, C.J., 1992. Waikite - Te Kopia the Missing Link? New Zealand Geothermal Workshop 1992 Proceedings.
Bromley, C.J., Hochstein, M.P., 2000. Heat transfer of the Karapiti fumarole field (1946–2000). Proceedings of the New Zealand Geothermal Workshop, pp. 87–92.
Brown, G., Rymer, H., Dowden, J., Kapadia, P., Stevenson, D., Barquero, J., Morales, L.D., 1989. Energy Budget Analysis for Poás Crater Lake: Implications for Predicting Volcanic Activity.
Dawson, G.B., 1964. The nature and assessment of heat flow from hydrothermal areas. N. Z. J. Geol. Geophys. 7, 155–171.
Dawson, G.B., Dickinson, D.J., 1970. Heat flow studies in thermal areas of the North Island of New Zealand. Geothermics 2, 466–473.
Fonstad, M.A., Dietrich, J.T., Courville, B.C., Jensen, J.L., Carbonneau, P.E., 2013. Topographic structure from motion: a new development in photogrammetric measurement. Earth Surf. Process. Landf. 38, 421–430. http://dx.doi.org/10.1002/esp.3366.
Fridriksson, T., Kristjánsson, B.R., Ármannsson, H., Margrétardóttir, E., Ólafsdóttir, S., Chiodini, G., 2006. CO_2 emissions and heat flow through soil, fumaroles, and steam heated mud pools at the Reykjanes geothermal area, SW Iceland. Appl. Geochem. 21, 1551–1569.
Glover, R.B., Klyen, L.E., Crump, M.E., 1992. Spring chemistry of the Waikite-Puakohurea thermal area. New Zealand Geothermal Workshop 1992 Proceedings.
Harris, A., 2013. Thermal Remote Sensing of Active Volcanoes: A User's Manual. Cambridge University Press.
Harvey, M.C., Pearson, S., Alexander, K.B., Rowland, J., White, P., 2014. Unmanned aerial vehicles (UAV) for cost effective aerial orthophotos and digital surface models (DSMs). New Zealand Geothermal Workshop 2014 Proceedings.
Harwin, S., Lucieer, A., 2012. Assessing the accuracy of georeferenced point clouds produced via multi-view stereopsis from unmanned aerial vehicle (UAV) imagery. Remote Sens. 4 (6), 1573–1599.
Healy, J., 1952. Waikite Hot Springs - to inspect the Waikite thermal area and assess its geothermal resources. DSIR Report, November 1952 (Rotorua).
McGonigle, A.J.S., Aiuppa, A., Giudice, G., Tamburello, G., Hodson, A.J., Gurrieri, S., 2008. Unmanned aerial vehicle measurements of volcanic carbon dioxide fluxes. Geophys. Res. Lett. 35 (6).
Muffler, P., Cataldi, R., 1978. Methods for regional assessment of geothermal resources. Geothermics 7 (2), 53–89.
NIWA, 2015. NIWA National Climate Database. http://cliflo.niwa.co.nz.
Nishar, A., Richards, S., Breen, D., Robertson, J., Breen, B., 2016. Thermal infrared imaging of geothermal environments by UAV (unmanned aerial vehicle). Journal of Unmanned Vehicle Systems 4 (2), 136–145.
Óladóttir, A.A., Friðriksson, Þ., 2015. The evolution of CO2 emissions and heat flow through soil since 2004 in the Utilized Reykjanes Geothermal Area, SW Iceland: ten years of observations on changes in geothermal surface activity. Proceedings World Geothermal Congress 2015, Melbourne, Australia.
O'Sullivan, M.J., Pruess, K., Lippmann, M.J., 2001. State of the art of geothermal reservoir simulation. Geothermics 30 (4), 395–429.
O'Sullivan, M.J., Yeh, A., Mannington, W.I., 2009. A history of numerical modelling of the Wairakei geothermal field. Geothermics 38 (1), 155–168.
Reeves, R.R., Power, J.F., Boothroyd, I.K.G., 2011. Waikite wetland restoration project: initial results. New Zealand Geothermal Workshop 2011 Proceedings.
Robert, C., Casella, G., 2013. Monte Carlo Statistical Methods. Springer Science & Business Media.
Sorey, M.L., Colvard, E.M., 1994. Measurements of heat and mass flow from thermal areas in Lassen Volcanic National Park, California, 1984–93 (No. 94-4180-A). US Geological Survey; USGS Earth Science Information Center, Open-File Reports Section.
Vilardo, G., Sansivero, F., Chiodini, G., 2015. Long-term TIR imagery processing for spatio-temporal monitoring of surface thermal features in volcanic environment: a case study in the Campi Flegrei (Southern Italy). J. Geophys. Res. Solid Earth 120 (2), 812–826.
Westoby, M.J., Brasington, J., Glasser, N.F., Hambrey, M.J., Reynolds, J.M., 2012. 'Structure-from-Motion' photogrammetry: a low-cost, effective tool for geoscience applications. Geomorphology 179, 300–314.